AD_____

Award Number: W81XWH-08-1-0353

TITLE: Optimization of Breast Tomosynthesis Imaging Systems for Computer-Aided Detection

PRINCIPAL INVESTIGATOR: Dr. Beverly Lau

CONTRACTING ORGANIZATION: University of Chicago
Chicago, IL 60637

REPORT DATE: May 2011

TYPE OF REPORT: Annual Summary

PREPARED FOR: U.S. Army Medical Research and Materiel Command
Fort Detrick, Maryland 21702-5012

REPORT DOCUMENTATION PAGE

Form Approved
OMB No. 0704-0188

1. REPORT DATE *(DD-MM-YYYY)*	2. REPORT TYPE	3. DATES COVERED *(From - To)*
01-05-2011	Annual Summary	1 MAY 2008-30 APR 2011

4. TITLE AND SUBTITLE

Optimization of Breast Tomosynthesis Imaging Systems for Computer-Aided Detection

5a. CONTRACT NUMBER

5b. GRANT NUMBER
W81XWH-08-1-0353

5c. PROGRAM ELEMENT NUMBER

6. AUTHOR(S)
Dr. Beverly Lau

E-Mail: beverly@uchicago.edu

5d. PROJECT NUMBER

5e. TASK NUMBER

5f. WORK UNIT NUMBER

7. PERFORMING ORGANIZATION NAME(S) AND ADDRESS(ES)
University of Chicago
Chicago, IL 60637

8. PERFORMING ORGANIZATION REPORT NUMBER

9. SPONSORING / MONITORING AGENCY NAME(S) AND ADDRESS(ES)
U.S. Army Medical Research and Materiel Command
Fort Detrick, Maryland 21702-5012

10. SPONSOR/MONITOR'S ACRONYM(S)

11. SPONSOR/MONITOR'S REPORT NUMBER(S)

12. DISTRIBUTION / AVAILABILITY STATEMENT
Approved for Public Release; Distribution Unlimited

13. SUPPLEMENTARY NOTES

14. ABSTRACT

The goal of this research is to develop methodology for optimizing acquisition parameters for digital tomosynthesis of the breast (DBT). Optimization is important to be able to study whether DBT can be used in place of screening mammography with better sensitivity and specificity. The research is composed of three parts: 1) to develop a computer model to simulate tomosynthesis, 2) to generate realistic breast and tumor models, and 3) to determine optimal acquisition parameters by using a genetic algorithm with CADe performance as an indicator of fitness. In this report, we summarize the research done for this project to date, focussing particularly on the development of an anthropomorphic software breast phantom and its validation. Lastly, we evaluate methods for measuring anatomic noise in projection imaging.

15. SUBJECT TERMS
Digital breast tomosynthesis, optimization, computer simulation, anatomic noise, anthropomorphic breast phantom

16. SECURITY CLASSIFICATION OF:			17. LIMITATION OF ABSTRACT	18. NUMBER OF PAGES	19a. NAME OF RESPONSIBLE PERSON
a. REPORT	b. ABSTRACT	c. THIS PAGE			USAMRMC
U	U	U	UU	30	19b. TELEPHONE NUMBER *(include area code)*

Contents

List of Figures

1 Introduction

This is the final report for this body of research.

Screen-film mammography and digital mammography have been used for over 30 years in the early detection of cancer. The combination of screening and adjuvant therapies have led to a decrease in the mortality rate from breast cancer [1]. Because mammography projects a three-dimensional object onto a two-dimensional surface, structures may be obscured by overlapping tissue, while simultaneously allowing overlapping normal tissue to appear tumor-like. A solution to this problem is digital breast tomosynthesis (DBT), which produces images of slices through the breast using multiple projection view images from a limited angular range [2, 3].

The goal of this research was to develop methodology for optimizing the acquisition parameters for tomosynthesis. This requires an understanding of the effect of individual acquisition parameters on image quality and on performance for search tasks in digital breast tomosynthesis. To accomplish this, we have developed a simulation for x-ray projection imaging, including ray tracing, focal spot blur, polychromaticity, scatter, quantum noise, and detector blur and noise. An existing digital anthropomorphic breast phantom was improved to include both large-scale and small-scale structures. We investigated methods for validating this phantom, including both spectral and computer-aided detection methods. We are currently validating this computer simulation, after which we plan on optimizing the acquisition parameters by exploring the surface of all possible combinations of acquisition parameters.

Since the start of this project, the Hologic digital breast tomosynthesis device has gained approval by the FDA, which occurred in February 2011. Other research groups have been working on the topic of optimization of different portions of the tomosynthesis imaging system [4–11]. Our group has also published on the effect of acquisition parameters and computer-generated quantum noise [12].

In the course of this research, we found it necessary to explore anthropomorphic software breast phantoms in greater depth. Anthropomorphic phantoms have become a bigger topic in the past decade. With the advent of three-dimensional imaging modalities and the decreasing cost of computer memory, it has become essential and feasible to create these multi-gigabyte arrays for the purpose of mimicking tissue in simulation studies. Many groups are working on creating breast phantoms, including ones based on mastectomy specimens [13], breast CT images [14], and entirely computer-generated models [15–19].

The only anthropomorphic physical breast phantom available for commercial sale is the "Rachel" breast phantom, developed by Caldwell and Yaffe [20]. Although the 2D projection views from this phantom are stunningly realistic; the anatomic noise of the phantom is contained in a single plane, which disallows its use in 3D imaging modalities. Recently, Carton and colleagues have developed a physical version of their software breast phantom [21]. The methods used to make a single phantom are time-consuming and costly, but the methods used (namely, rapid prototyping) has potential to be useful in future studies where a physical phantom is needed to correspond exactly to a software one.

This final report will summarize the research accomplished during the entire period of this award, including the work done on anthropomorphic phantoms, which has become a big portion of this research.

2 Body

The statement of work associated with this research included three parts:

1. To develop a computer model to simulate a clinical DBT system
2. To develop a theoretical framework to determine optimal acquisition conditions
3. To test the simulated DBT images using CADe packages

We have completed the assembly of the computer model simulation of the clinical DBT system. This simulation includes Monte Carlo-derived point response functions for detector simulation as well as similarly-derived scatter point spread functions for scatter simulation. The model also includes focal spot blur, inverse-square law, polychromaticity, quantum noise, detector blur, and detector noise.

2.1 To develop a computer model to simulate a clinical DBT system

The computer model was completed in 2010, and subsequent work was done to validate this simulation. In this section, I will describe the architecture of the code and I will explain the extent of the validation we have performed so far.

Each physical factor can be independently included or removed from the simulation, so that each parameter can be tested for its effect on the final image quality. To visualize the architecture of the program, see Appendix A.

2.1.1 Simulation

A.1. Focal spot blur: The focal spot is simulated as a superposition of multiple images, each made with an infinitesimal point source distributed over an area equivalent to the size of the focal spot. Since the x-ray source is identical between the GE Senographe Essential and the GE tomosythesis prototype, we measured the size of the focal spot of the GE Senographe Essential in order to estimate the actual size of the tomosynthesis system focal spot. A 30-micron pinhole was used to measure the focal spot size for two nominal sizes (100 microns and 300 microns) (see Table 1).

Knowing the actual size of the focal spot enables us to choose source points that capture the extent of the focal spot. The number of focal spot points is defined by four parameters: the length and width of the spot, as well as the number of grid points in each of two directions. The simulation will then generate an array of points that span the space, and a projection is calculated for each point, which are summed together to produce the blurring effect.

Table 1: Measured sizes for two focal spots on the GE Senographe Essential.

Nominal size	Actual size (microns)	
	$\perp$ to A/C†	$\parallel$ to A/C
100 microns	177.75	236.38
300 microns	591.83	497.35

† A/C is the anode-cathode axis.

A.2. Angle-dependent scatter: Scatter was modeled as a change in resolution and magnitude of the image. Scatter point spread functions (sPSFs) were measured using a Monte Carlo software package called PENELOPE [22], which simulates gamma and electron/positron interactions to generate particle track maps as well as dose distributions.

Geometries for these scenarios were defined using quadric surfaces, and sPSFs were generated assuming an ideal detector at a distance 1 cm below a 5-cm thick infinitely long volume of 50-50 glandular-adipose tissue. In the future, new point spread functions should be made for different thicknesses and different air gaps.

Scatter point spread functions were generated for angles of incidence ranging from 0 degrees to +60 degrees. These sPSFs were reflected in order to obtain sPSFs for -60 degrees to 0 degrees incidence.

We validated our sPSFs by comparing the data for zero degrees to data from Boone *et al.* [23]. We also compared our non-zero degree incidence sPSFs to data from Sechopoulos *et al.* [24] We found good agreement in both cases. These methods and results are described in the Annual Grant Update from 2009 [25].

A.3. Angle-dependent detector response: Two different detectors were modeled: gadolinium oxysulfide (Gd_2O_2S) and cesium iodide (CsI). The Gd_2O_2S detector was modeled by summing together Gaussian point response functions, one for each layer of the detector. The depth-dependent MTF was determined using an equation from Nishikawa and Yaffe [26]. The CsI detector was modeled using depth-dependent point response functions (PRFs), which were computed using a Monte Carlo simulation package called MANTIS. MANTIS works in conjunction with PENELOPE to convert the absorbed dose into detector output for an indirect detector. MANTIS models optical photon interactions, taking into account the surface reflective properties of the materials in the geometry. To obtain depth-dependent PRFs, x-ray photons were forced to interact at a certain depth below the top surface of the detector. This method is described in the Annual Grant Update from 2010 [27].

The detector PRFs were acquired on a 300 micron x 300 micron square detector, with a resolution of 1 micron. While this produced very nice images of PRFs, convolution at such a high resolution was too memory intensive to carry out. For this reason, we down-sampled the PRFs to 10-micron pixel size, which retained good spatial resolution while reducing the amount of memory needed.

In future studies, we found that even the 10-micron pixel size required too much memory to perform the convolution operation with the projection view image. Since we are modeling a GE-prototype tomosynthesis system, and the GE detector has a final resolution of 100 microns, the detector-blurred image would eventually need to be down-sampled to 100 microns. For a one-dimensional pattern, we did the down-sampling both before and after a 1D convolution (with a low-resolution and a high-resolution PRF, respectively). We found small differences between the two cases, which led us to conclude that there would be little difference if we performed the down-sampling before convolution. The 10-micron PRFs were down-sampled further to 100 microns, which gave very coarse point response functions with matrix size 3x3.

A.4. Detector types: We modeled two detector types: gadolinium oxysulfide and cesium iodide, as described in the previous section.

2.1.2 DBT system parameters

B.1. Geometries We have simulated just the partial isocentric geometry so far. The projection code we have written, however, includes framework for easily switching over to different geometries, such as circular and linear. This particular experiment was limited to a single geometry because the scatter point spread functions we generated were strictly for a 1-cm air gap between the scattering material and the detector surface. For circular geometry, the air gap linearly increases across the detector, leading to a variable sPSF, which cannot be modeled using linear shift invariant techniques, as we have done here.

B.2. Acquisition parameters

B.2.1. Number of projection views: We have investigated the effect of number of projection views on detectability of microcalcification-like spheres embedded in 50-50 glandular-adipose breast tissue. Using a fixed angular range, we varied the number of projection views and calculated the detectability of microcalcifications in the projection view and reconstructed slices using template matching in a signal-known exactly task. We concluded that any number of projection views greater than 11 does not affect the detectability of microcalcifications; however, fewer than 11 projection views detrimentally affects detectability. This data was presented at the SPIE Medical Image scientific meeting in 2008, and it is reported in the Annual Grant Update from 2009 [25].

B.2.2. Angular range: In that same study, we also varied the angular range while keeping the number of views fixed at 11. We found that an increased angular range actually decreases detectability of microcalcifications, when the number of views is held constant. Similarly to the number of projection views study, we only included quantum noise in the projection view images, since the scatter and detector models had not been completed at the time. Again, this data is contained in the Annual Grant Update from 2009 [25].

B.2.3. Dose distribution: We have evaluated the effect of a variable exposure method, which placed half the x-ray photons in the middle projection view, while dividing the other half of the exposure among the remaining projection views. In this study, we again only included quantum noise. We found that, although the detectability index is very high in the middle projection, the other projection views have such a decreased detectability, that it negatively affects the overall detectability once the projections are reconstructed into slices through the breast. This data was presented at the AAPM Annual Meeting in 2008, and the data can be found in the Annual Grant Update from 2009 [25].

B.2.4. Total dose: We have not yet evaluated the effect of total dose on the image quality of tomosynthesis.

B.2.5. Angular distribution of projection views: We have not explicitly studied the effect of the angular distribution of projection views; however, the simulation has been designed so that such a study can easily be accommodated. The framework exists for controlling the angular spacing between projection views. Also, we plan on acquiring data for all views, then manually selecting views to combine in order to simulate the non-uniform distribution.

B.2.6. Beam quality: We have measured scatter point spread functions for monoenergetic beams between 12 and 40 keV. Using these monoenergetic sPSFs, we can generate sPSFs for any spectrum up to 40 kVp, using weights for each sPSF based on the shape of the spectrum. So far, this has been done for a molybdenum anode and molybdenum filter.

We have collected x-ray spectra for a variety of anodes and filters, using code developed by John Boone. We have produced x-ray spectra that range from 24 kVp to 40 kVp for anode-filter combinations including Mo-Mo, Mo-Rh, and Rh-Rh. These combinations were selected because they represent the possible configurations that the GE Senographe Essential digital mammography unit can achieve.

2.1.3 Validation

Although validation was not included in the original proposal, it became clear that such a step was necessary. For validation, we imaged a lead edge on the GE Senographe Essential digital mammography unit. It was difficult to match the simulation to the acquired data because the distances among the source, the edge, and the detector were not easy to measure with great accuracy. To alleviate this problem, we used the PENELOPE Monte Carlo code to simulate the projection of a lead edge onto the detector, using a cone beam and a monoenergetic beam.

For the Monte Carlo simulation, we simulated an x-ray system with the source 66 cm above the center of a 5 cm x 5 cm detector. The x-ray source was defined to produce a cone beam with angular span of 8 degrees, which was able to deliver primary x rays to every point on the detector. The lead edge was constructed to be 0.060 inches (0.1524 cm) thick and 2 inches by 2 inches in length and width, which is identical to the physical lead edge we have in our lab. The attenuating material simulated was a 10 cm by 10 cm Lucite block, with a thickness of 4.68 cm, which is also identical to a physical block of Lucite in our lab. The Lucite was placed 1 cm above the detector plane, and the lead edge was placed 6 cm above the detector, on the source side. The lead edge was aligned so that it was at the center of the cone beam, parallel to the anode-cathode axis. It was later noticed that the cone beam led to artifacts at the edges of the detector, so a larger cone beam was used, and a collimator was inserted into the simulation at 7 cm above the detector. The collimator was chosen to be lead with

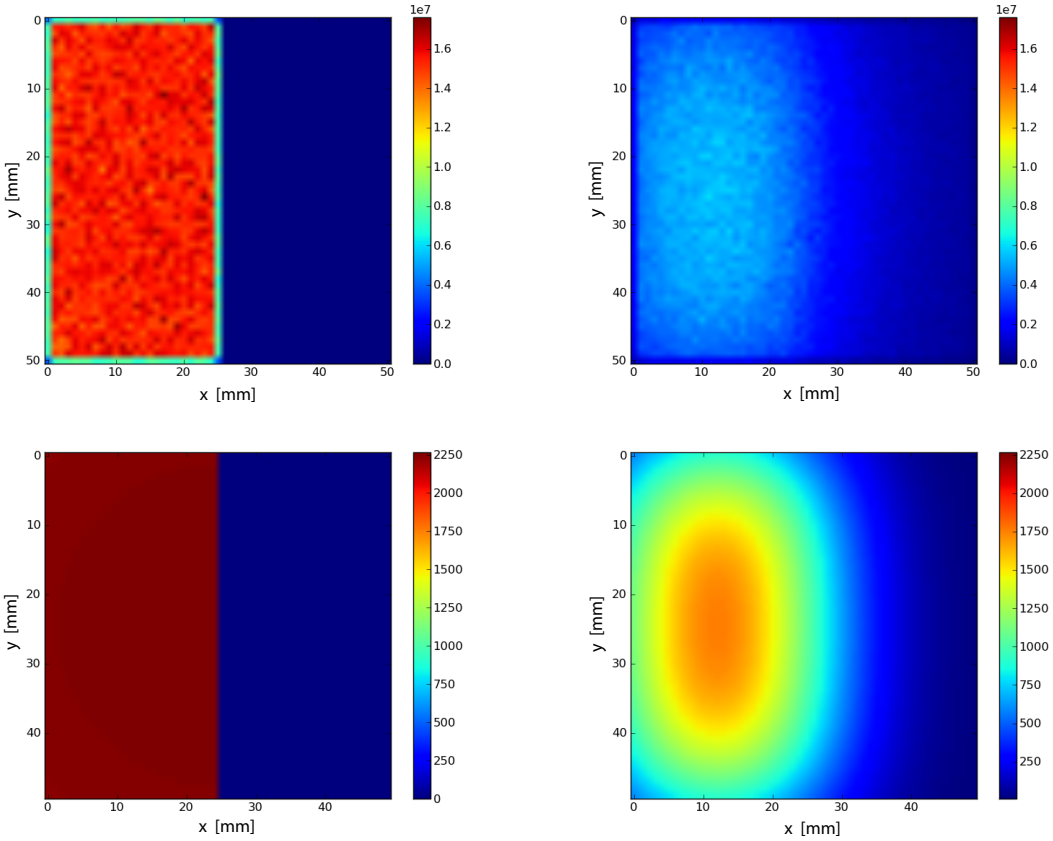

Figure 1: Comparison of PENELOPE and our tomosynthesis projection simulation with physical effects included. Top row: PENELOPE Monte Carlo simulation, bottom row: our tomosynthesis simulation. Left column is the primary-only image, right column is the scatter-only image. The magnitudes do not match because the Monte Carlo simulation is presented in energy, while the simulation is presented in number of photons.

0.2 cm thickness, with a window 5 cm x 5 cm in size.

We were able to match the tomosynthesis simulation (for zero degrees) to this Monte Carlo projection. In particular, the edge has very similar shape characteristics between the two simulations (see Figs. 1 and 2). Since PENELOPE has been validated multiple times by other groups, we accept this match as a good indicator that our simulation is performing adequately.

2.2 To develop a theoretical framework to determine optimal acquisition conditions

In order to construct a proper test for optimal acquisition parameters, it was necessary to explore computer breast phantoms that would be able to provide realistic 3D breast structure for clinically relevant tasks, such as detecting a tumor in a structured background. We will obtain model software lesions from Luis de Sisternes at IIT [28], and these lesions will be embedded into the breast phantoms for projection. This portion of the study has not been completed yet.

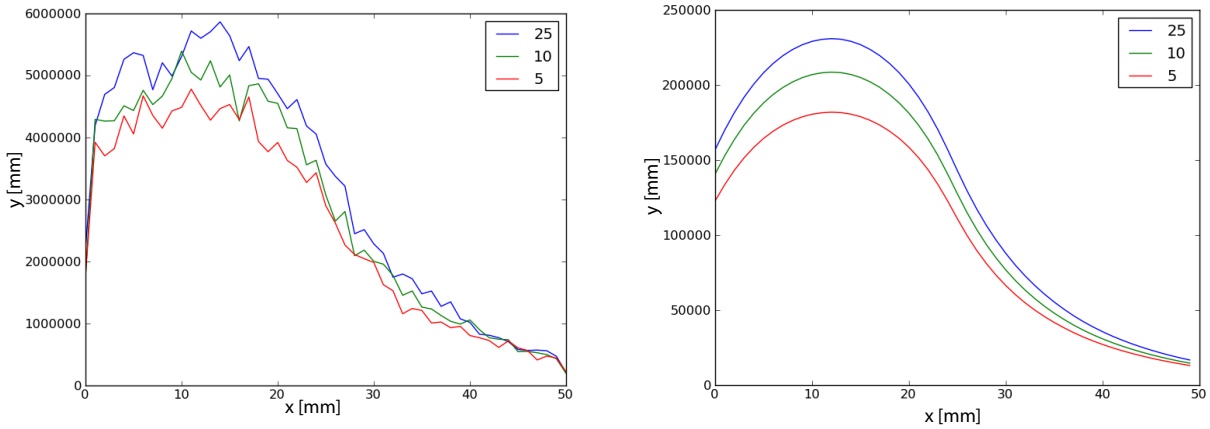

Figure 2: Line profiles through y=5, y=10, y=25 of the scatter-only images in Fig. 1. The PENELOPE Monte Carlo simulation data is on the left, and the tomosynthesis simulation data is on the right.

2.2.1 An anthropomorphic breast phantom

We worked in collaboration with Predrag Bakic and colleagues at the University of Pennsylvania to develop an anthropomorphic software breast phantom. The software breast phantom was written in a combination of C and Matlab, and it consisted of region growing from randomly chosen seed points in a half-ellipsoid shape. This phantom is described in the literature [16–19].

The phantom generally was comprised of compartments that were assigned to be either glandular or adipose. The connective tissue between these compartments corresponded to Cooper's ligaments. The user can specify the total percent glandular tissue desired, as well as the physical dimensions of the ellipsoid in which the breast is contained. At the center of the breast was a "predominantly glandular" area, which amounted to a volume shaped like a heart. The user can also control the extent of this volume in three directions.

In its original formulation (call this "Phantom I"), these compartments were sometimes very spherical, and they all had very prominent edges. The most unrealistic aspect of the phantom was the "predominantly glandular" area of the breast, which had extremely prominent edges that were readily apparent in the projection view images.

To correct the problems with prominent edges, a phantom was created to have zero percent glandular tissue and a very small "predominanty glandular" region. (It was impossible to make this volume non-existent.) Some of the empty adipose compartments were then filled with filtered noise, and the whole image was blurred with a Gaussian (to reduce step-like edges) and linearly interpolated so that the phantom had voxel sizes 100 micron x 100 micron x 100 micron. Call this "Phantom II" to avoid confusion.

2.2.2 Validation of phantoms

Validation of these phantoms was not a part of the original proposal, but we found that it was necessary in order to make any claims about the results at the end of the optimization. In order to show that these phantoms could be used as a surrogate for real breast tissue, we performed spectral analysis on regions of interest extracted from the projected images (as well as the reconstructed slices). We measured the quantity β, which is the slope of radially averaged squared modulus of the 2D power spectrum

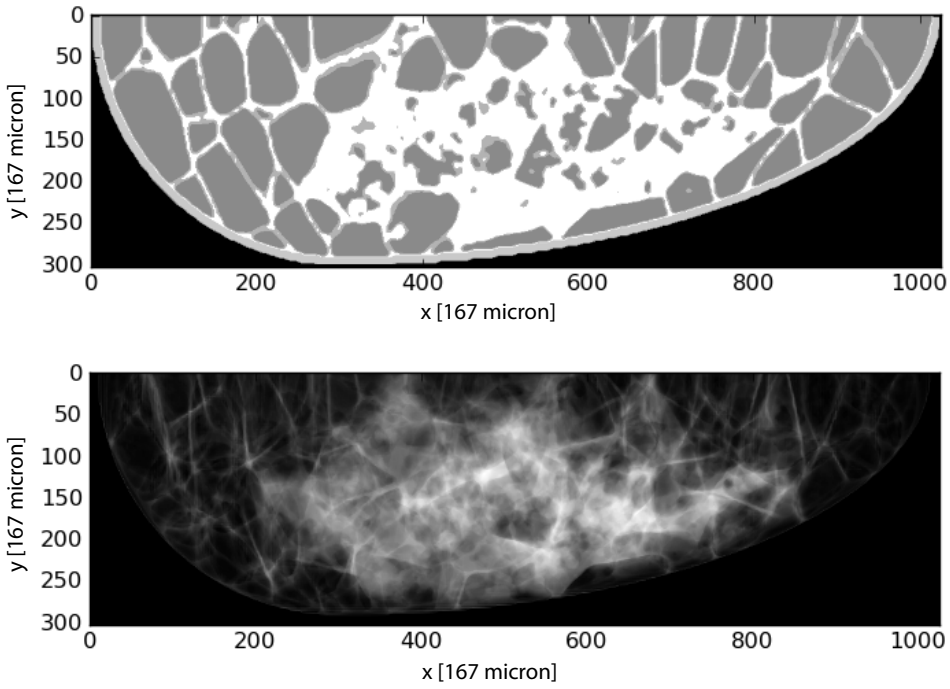

Figure 3: A slice from Phantom II (top) and a parallel beam projection (bottom). Phantom II is an improved anthropomorphic software breast phantom, with two glandular tissue types and 0.5-mm Cooper's ligaments.

for each ROI. From the literature, β has been shown to be about 3 for mammography and clinical breast tomosynthesis images. We found β for the phantom images to be comparable. The methods and results for these experiments were presented at IWDM 2010 and AAPM 2010. The proceedings paper and supplemental abstract for both, respectively, can be found as appendices to the Annual Grant Update from 2010 [27]. Although this is necessary for showing that the phantoms are realistic, it is not sufficient, since many things in nature exhibit power spectral slopes of approximately 3. We plan to perform a study showing that the number of false positives obtained in a clinically relevant task is similar between phantom images and clinical images.

One caveat of the studies we performed was that Phantom I could only be made with a voxel size of (500 microns)^3 (within reasonable calculation time and memory). We discovered that projecting a 500-micron phantom onto a 100-micron detector led to artifacts in the periodograms (see Fig. 4), so we were restricted to projecting the 500-micron phantoms onto 500-micron detectors. In order to extract ROIs with enough pixels for spectral analysis, we sampled regions that were much larger (3.2 cm x 3.2 cm) than the regions sampled in the clinical cases we were comparing (1 cm x 1 cm). When the clinical cases were sampled with a 3.2 cm ROI, we noticed that our data looked very similar to the phantom data, which led us to believe that the differences were a result of the ROI size choice.

We compared a few different methods for testing the effect of ROI size on calculation of β. These methods and results were presented at the SPIE Medical Imaging meeting in 2011, and the accompanying proceedings paper can be found as Appendix B. We concluded that β is not affected by ROI size if the ROI is greater than 2.5 cm x 2.5 cm. We hypothesize that the case may be that there are structures in the breast that can be entirely captured in ROIs that are big enough. If the ROI is too small, these structures may be partitioned, thus contributing to the power spectra in unpredictable ways.

2.3 To test the simulated DBT images on CADe packages

We have begun looking at the radial gradient index for the simulated phantom images, which is described in the Annual Grant Update from 2010 [27]. We have not performed the optimization study, but we have discussed methods for moving forward, including strategies for generating phantoms in parallel on our new Cray supercomputer, embedding lesions into the phantoms, and evaluating results from the CADe scheme.

3 Key research accomplishments

2009

- Developed framework for tomosynthesis computer simulation
- Showed PENELOPE Monte Carlo package is able to reproduce scatter data produced using Geant4 from the Sechopoulos group.
- Developed methods for implementing scatter in the computer model
- Showed the relationship between detectability and both number of projection views and angular range for Poisson noise only.
- Showed that variable exposure, without detector physics other than Poisson noise, causes lower detectability of microcalcifications in the reconstructed image with larger number of projection views.

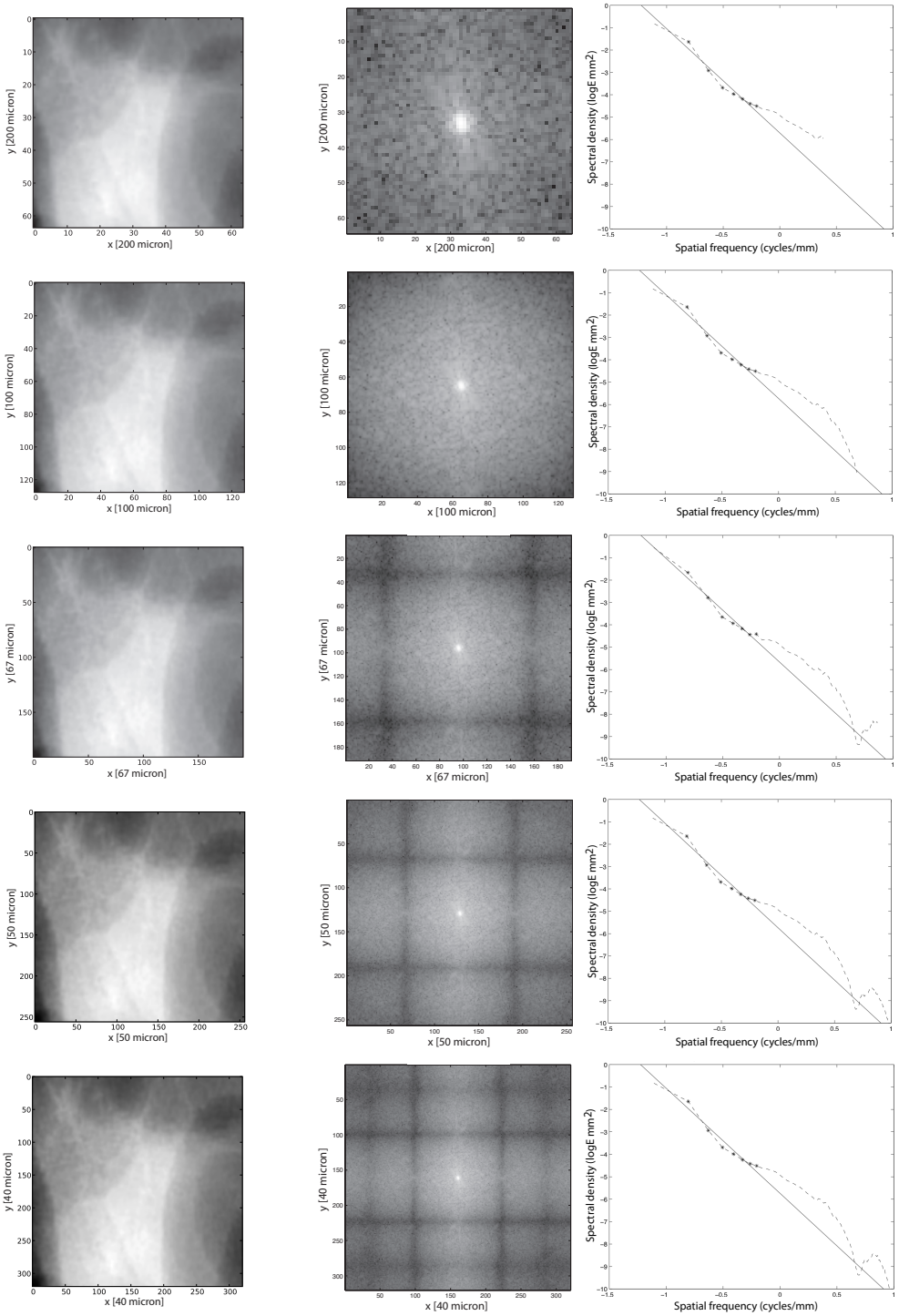

Figure 4: Projection of 200-micron voxel 10-percent-density phantom onto detectors of different pixel sizes. From top to bottom, 200-micron, 100-micron, 67-micron, 50-micron, and 40-micron. ROI size was selected so that detector area was constant, 1.28 cm x 1.28 cm. This corresponded to the following ROI sizes: 64, 128, 191, 256, 320, respectively. Left to right: image of projected ROI, periodogram, and power spectrum.

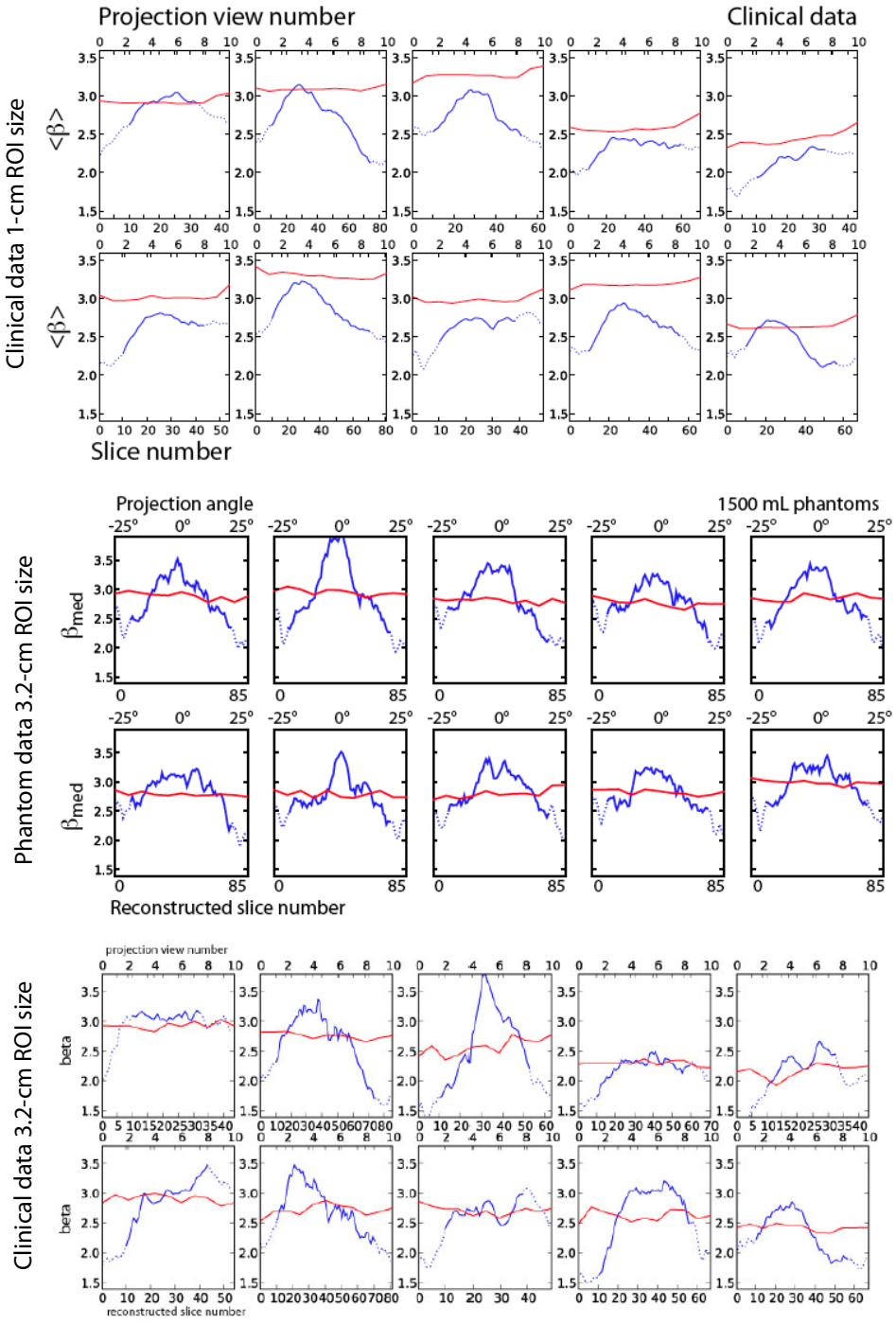

Figure 5: Comparison of clinical and phantom data using different ROI sizes. Top: β values for projection view and reconstructed slices for 100-micron ROIs from ten clinical cases; middle: β values for 320-micron ROIs from ten phantoms; bottom: β values for 320-micron ROIs from ten clinical cases (same cases as above). In each set of data, the red line corresponds to average β measured across projection view images, and the blue line corresponds to average β measured across reconstructed slices. Reconstruction was done with 8-iteration MLEM.

2010

- Improved framework for tomosynthesis computer simulation by implementing the concept of a "master layer", which decreases the amount of time for projection by a factor of the number of layers in the detector (on the order of 100-200).
- Calculated point response functions for oblique angles of incidence on a cesium iodide detector.
- Demonstrated that the point response functions generated can be used in place of Monte Carlo simulation for detector modeling, reducing computation time from 20 hours to about 1 second.
- Measured anatomic noise for anthropomorphic breast phantoms we plan to use in our optimization study. Showed that this anatomic noise is comparable to that in clinical tomosynthesis breast images.

2011

- Demonstrated spectral agreement in reconstructed slices between our phantom (Phantom I) and clinical tomosynthesis data.
- Demonstrated that ROI size used to evaluate breast tissue structure affects spectral analysis for small enough ROI sizes.
- Improved an anthropomorphic software breast phantom to look more realistic.
- Partially validated our simulation code by comparing results for a single situation with data from Monte Carlo simulations.

4 Reportable outcomes

4.1 Abstracts

- BA Lau, IS Reiser, RM Nishikawa, "The effect of variable exposure on microcalcification detectability in tomosynthesis." Medical Physics **35**:6 p2978, June 2008.
- IS Reiser, RM Nishikawa, BA Lau, "Effect of non-isotropic detector blur on microcalcification detectability in tomosynthesis." Proceedings of SPIE **7258**: 72585Z, Feb 2009.
- BA Lau, PR Bakic, I Reiser, A-K Carton, ADA Maidment, RM Nishikawa, "An Anthropomorphic Software Breast Phantom for Tomosynthesis Simulation: Power Spectrum Analysis of Phantom Reconstructions." Medical Physics, June 2010.

4.2 Presentations

- BA Lau, IS Reiser, RM Nishikawa, "Microcalcification detectability in tomosynthesis." 2008 NIBIB Training Grantee Meeting in Silver Spring, MD.
- BA Lau, IS Reiser, RM Nishikawa, "The effect of variable exposure on microcalcification detectability in tomosynthesis." 2008 AAPM Annual Meeting in Houston, TX.
- IS Reiser, RM Nishikawa, BA Lau, "Effect of non-isotropic detector blur on microcalcification detectability in tomosynthesis." 2009 SPIE Medical Imaging Meeting in Orlando, FL.

- PR Bakic, BA Lau, A-K Carton, I Reiser, ADA Maidment, RM Nishikawa, "An Anthropomorphic Software Breast Phantom for Tomosynthesis Simulation: Power Spectrum Analysis of Phantom Projections." International Workshop on Digital Mammography in Girona, Spain. June 17, 2010.
- BA Lau, PR Bakic, I Reiser, A-K Carton, ADA Maidment, RM Nishikawa, "An Anthropomorphic Software Breast Phantom for Tomosynthesis Simulation: Power Spectrum Analysis of Phantom Reconstructions." AAPM Annual Meeting in Philadelphia, PA. July 22, 2010.
- B. A. Lau, I. Reiser, R. Nishikawa, "Issues in characterizing anatomic structure in digital breast tomosynthesis," presented at SPIE Medical Imaging, Orlando, FL, February 12-17, 2011.

4.3 Proceedings papers

- PR Bakic, BA Lau, A-K Carton, I Reiser, ADA Maidment, RM Nishikawa, "An Anthropomorphic Software Breast Phantom for Tomosynthesis Simulation: Power Spectrum Analysis of Phantom Projections." Lecture Notes in Computer Science 6316, 452-458 (2010).
- BA Lau, I Reiser and RM Nishikawa, "Issues in characterizing anatomic structure in digital breast tomosynthesis", Proc. SPIE 7961, 796113 (2011).

5 Conclusions

From these experiments, we have explored some of the parameters that will be essential for optimizing digital breast tomosynthesis. The computer simulation and the methodology we have developed may be used for other imaging modalities that use projection x rays as the fundamental source of contrast. In addition to the experiments proposed, we have performed extensive research on anthropomorphic software breast phantoms, and we have produced a phantom that appears realistic in projection view images. We have also investigated methods for validation of these phantoms — namely, calculation of β, a description of the amount and type of anatomic noise — that have only recently been studied by other groups. It is our hope that future generations of researchers will follow suit in evaluating the materials they use before planning elaborate studies, only to find that the premise was unrealistic at the start.

References

[1] D. A. Berry, K. A. Cronin, S. K. Plevritis, D. G. Fryback, L. Clarke, M. Zelen, J. S. Mandelblatt, A. Y. Yakovlev, J. D. F. Habbema, E. J. Feuer, C. Intervention, and S. M. N. C. Collaborators, "Effect of screening and adjuvant therapy on mortality from breast cancer," *N Engl J Med* **353**, pp. 1784–92, Oct 2005.

[2] L. T. Niklason, B. T. Christian, L. E. Niklason, D. B. Kopans, D. E. Castleberry, B. H. Opsahl-Ong, C. E. Landberg, P. J. Slanetz, A. A. Giardino, R. Moore, D. Albagli, M. C. DeJule, P. F. Fitzgerald, D. F. Fobare, B. W. Giambattista, R. F. Kwasnick, J. Liu, S. J. Lubowski, G. E. Possin, J. F. Richotte, C. Y. Wei, and R. F. Wirth, "Digital tomosynthesis in breast imaging," *Radiology* **205**, pp. 399–406, Nov 1997.

[3] T. Wu, A. Stewart, M. Stanton, T. McCauley, W. Phillips, D. B. Kopans, R. H. Moore, J. W. Eberhard, B. Opsahl-Ong, L. Niklason, and M. B. Williams, "Tomographic mammography using a limited number of low-dose cone-beam projection images," *Medical physics* **30**, pp. 365–80, Mar 2003.

[4] J. Zhou, B. Zhao, and W. Zhao, "A computer simulation platform for the optimization of a breast tomosynthesis system," *Medical physics* **34**, pp. 1098–109, Mar 2007.

[5] H. Gifford, C. Didier, M. Das, and S. Glick, "Optimizing breast-tomosynthesis acquisition parameters with scanning model observers," *Proceedings of SPIE* **6917**, p. 69170S, 2008.

[6] R. Saunders, E. Samei, C. Badea, H. Yuan, K. Ghaghada, Y. Qi, L. Hedlund, and S. Mukundan, "Optimization of dual energy contrast enhanced breast tomosynthesis for improved mammographic lesion detection and diagnosis," *Proceedings of SPIE* **6913**, p. 69130Y, 2008.

[7] R. S. Saunders, E. Samei, J. Y. Lo, and J. A. Baker, "Can compression be reduced for breast tomosynthesis? monte carlo study on mass and microcalcification conspicuity in tomosynthesis," *Radiology* **251**, pp. 673–82, Jun 2009.

[8] A. Chawla, J. Lo, J. Baker, and E. Samei, "Optimized image acquisition for breast tomosynthesis in projection and reconstruction space," *Medical physics* **36**, p. 4859, 2009.

[9] A. Svalkvist and M. Båth, "Simulation of dose reduction in tomosynthesis," *Medical physics* **37**, pp. 258–69, Jan 2010.

[10] T. Mertelmeier, J. Ludwig, B. Zhao, and W. Zhao, "Optimization of tomosynthesis acquisition parameters: angular range and number of projections," *Digital Mammography* **5116**, pp. 220–227, 2010.

[11] I. Sechopoulos and C. Ghetti, "Optimization of the acquisition geometry in digital tomosynthesis of the breast," *Medical Physics* **36**, pp. 1199–1207, Mar 2009.

[12] I. Reiser and R. M. Nishikawa, "Task-based assessment of breast tomosynthesis: Effect of acquisition parameters and quantum noise," *Medical physics* **37**, p. 1591, Jan 2010.

[13] J. O'Connor, M. Das, C. Didier, M. Mah'D, and S. Glick, "Development of an ensemble of digital breast object models," *Digital Mammography* **6136**, pp. 54–61, 2010.

[14] C. Li, W. Segars, G. Tourassi, J. Boone, and J. D. III, "Methodology for generating a 3d computerized breast phantom from empirical data," *Medical physics* **36**, p. 3122, 2009.

[15] B. Chen, J. Shorey, and R. S. Jr. . . , "An anthropomorphic breast model for breast imaging simulation and optimization.," *Academic . . .* **18**, Jan 2011.

[16] P. R. Bakic, M. Albert, D. Brzakovic, and A. D. A. Maidment, "Mammogram synthesis using a 3D simulation. I. Breast tissue model and image acquisition simulation," *Medical physics* **29**, pp. 2131–9, Sep 2002.

[17] P. R. Bakic, M. Albert, D. Brzakovic, and A. D. A. Maidment, "Mammogram synthesis using a 3D simulation. II. Evaluation of synthetic mammogram texture," *Medical physics* **29**, pp. 2140–51, Sep 2002.

[18] P. R. Bakic, M. Albert, D. Brzakovic, and A. D. A. Maidment, "Mammogram synthesis using a three-dimensional simulation. III. Modeling and evaluation of the breast ductal network," *Medical physics* **30**, pp. 1914–25, Jul 2003.

[19] C. Zhang, P. R. Bakic, and A. D. A. Maidment, "Development of an anthropomorphic breast software phantom based on region growing algorithm," *Proc. SPIE* **6918**(69180V), 2008.

[20] C. Caldwell and M. Yaffe, "Development of an anthropomorphic breast phantom," *Medical physics* **17**, p. 273, 1990.

[21] A.-K. Carton, P. Bakic, C. Ullberg, H. Derand, and A. D. A. Maidment, "Development of a physical 3d anthropomorphic breast phantom," *Medical physics* **38**, p. 891, Jan 2011.

[22] F. Salvat, J. Fernandez-Varea, and J. Sempau, "PENELOPE-2006: A Code System for Monte Carlo Simulation of Electron and Photon Transport," *Nuclear Energy Agency* , p. 293, Jun 2006.

[23] J. M. Boone and V. N. Cooper, "Scatter/primary in mammography: Monte Carlo validation," *Medical physics* **27**, pp. 1818–31, Aug 2000.

[24] I. Sechopoulos, S. Suryanarayanan, S. Vedantham, C. J. D'Orsi, and A. Karellas, "Scatter radiation in digital tomosynthesis of the breast," *Med Phys* **34**, pp. 564–576, Jan 2007.

[25] B. A. Lau, "Annual grant update," 2009.

[26] R. M. Nishikawa and M. J. Yaffe, "Model of the spatial-frequency-dependent detective quantum efficiency of phosphor screens," *Medical physics* **17**, pp. 894–904, Jan 1990.

[27] B. A. Lau, "Annual grant update," 2010.

[28] L. de Sisternes, A. M. Zysk, J. G. Brankov, and M. N. Wernick, "Development of a computational three-dimensional breast lesion phantom model," *Proc. SPIE* **7622**, pp. 762205–762205–8, 2010.

A Simulation code flowchart

See the following two pages for a schematic of the simulation code.

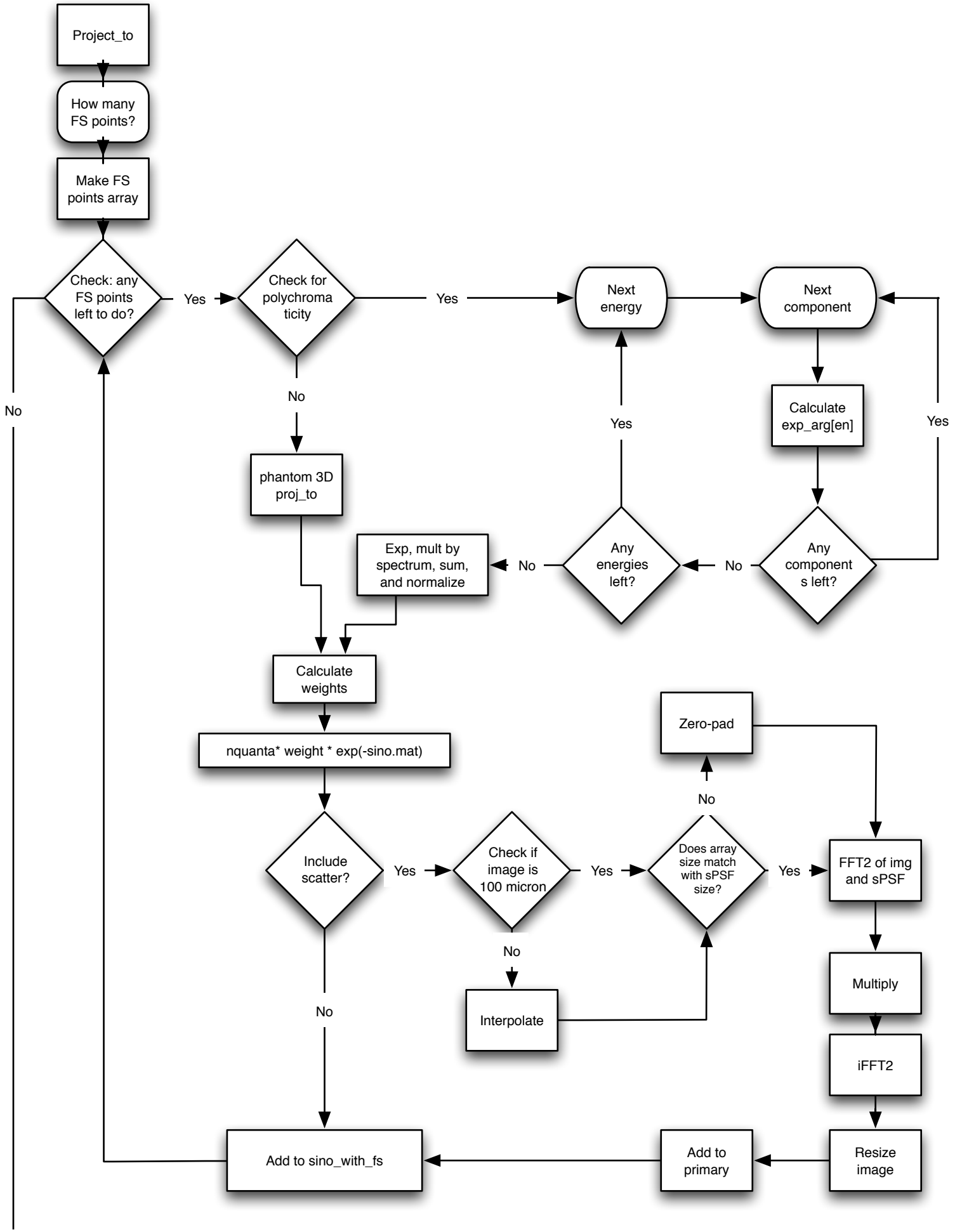
Project_to
How many FS points?
Make FS points array
Check: any FS points left to do?
Yes
No
Check for polychromaticity
Yes
No
Next energy
Next component
Calculate exp_arg[en]
Yes
Yes
Any energies left?
No
Any components left?
No
Exp, mult by spectrum, sum, and normalize
phantom 3D proj_to
Calculate weights
nquanta* weight * exp(-sino.mat)
Include scatter?
Yes
No
Check if image is 100 micron
Yes
No
Interpolate
Does array size match with sPSF size?
Yes
No
Zero-pad
FFT2 of img and sPSF
Multiply
iFFT2
Resize image
Add to primary
Add to sino_with_fs

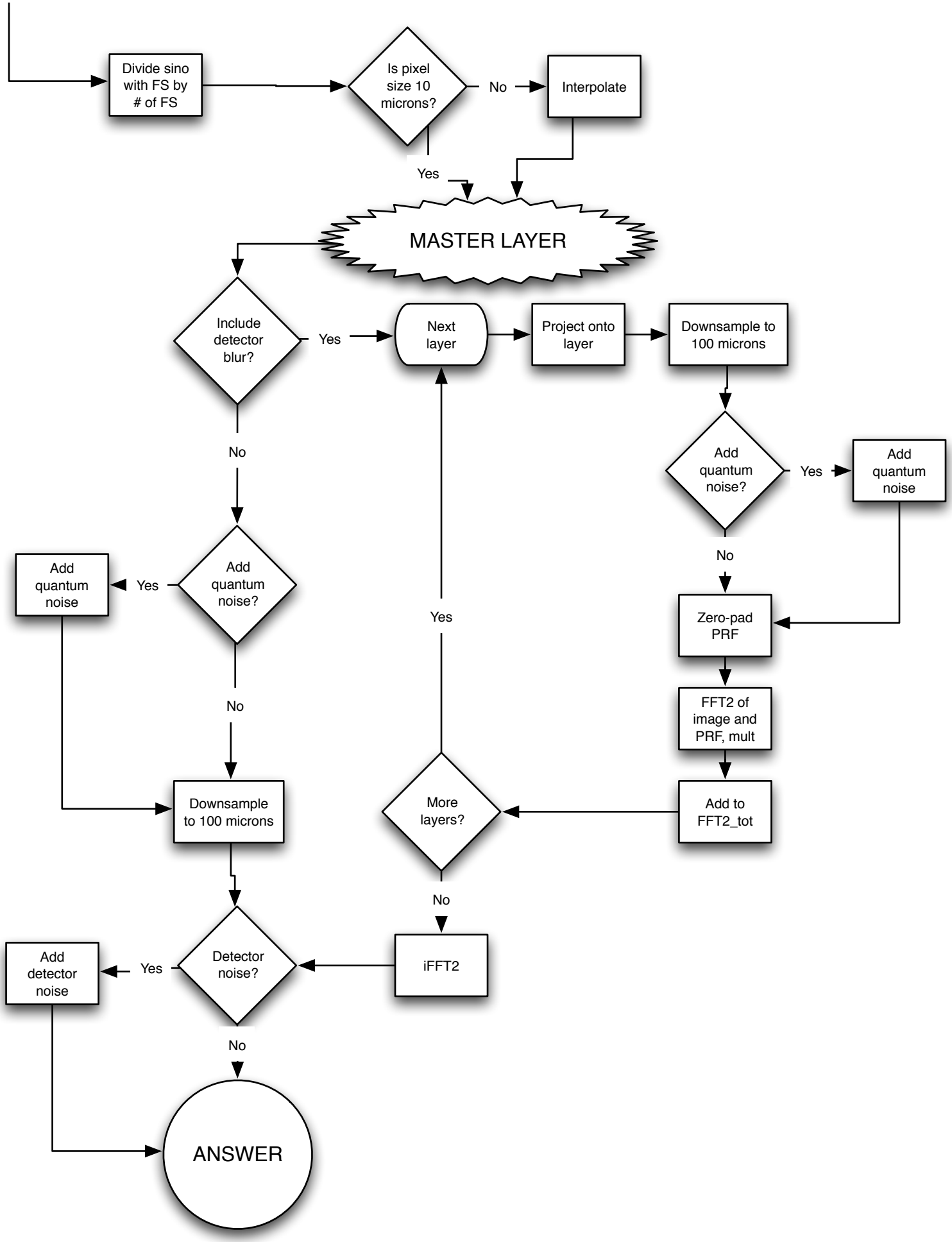
Divide sino with FS by # of FS
Is pixel size 10 microns?
No
Interpolate
Yes
MASTER LAYER
Include detector blur?
Yes
Next layer
Project onto layer
Downsample to 100 microns
Add quantum noise?
Yes
Add quantum noise
No
Zero-pad PRF
FFT2 of image and PRF, mult
Add to FFT2_tot
More layers?
Yes
No
iFFT2
Detector noise?
Yes
Add detector noise
No
ANSWER
Add quantum noise?
Yes
Add quantum noise
No
Downsample to 100 microns

B SPIE 2011 Proceedings Paper

Title: Issues in characterizing anatomic structure in digital breast tomosynthesis.
Authors: BA Lau, I Reiser, RM Nishikawa

Normal mammographic backgrounds have power spectra that can be described using a power law $P(f) = c/f^{\beta}$, where β ranges from 1.5 to 4.5. Anatomic noise can be the dominant noise source in a radiograph. Many researchers are characterizing anatomic noise by β, which can be measured from an image. We investigated the effect of sampling distance, offset, and region of interest (ROI) size on β. We calculated β for tomosynthesis projection view and reconstructed images, and we found that ROI size affects the value of β. We evaluated four different square ROI sizes (1.28, 2.56, 3.2, and 5.12 cm), and we found that the larger ROI sizes yielded larger β values in the projection images.

The β values change rapidly across a single projection view; however, despite the variation across the breast, different sampling schemes (which include a variety of sampling distances and offsets) produced average β values with less than 5% variation. The particular location and number of samples used to calculate β does not matter as long as the whole image is covered, but the size of the ROI must be chosen carefully.

See attached.

Issues in characterizing anatomic structure in digital breast tomosynthesis

Beverly A. Lau, Ingrid Reiser, Robert M. Nishikawa

The University of Chicago, Department of Radiology, Chicago, IL, USA

ABSTRACT

Normal mammographic backgrounds have power spectra that can be described using a power law $P(f) = c/f^{\beta}$, where β ranges from 1.5 to 4.5. Anatomic noise can be the dominant noise source in a radiograph. Many researchers are characterizing anatomic noise by β, which can be measured from an image. We investigated the effect of sampling distance, offset, and region of interest (ROI) size on β. We calculated β for tomosynthesis projection view and reconstructed images, and we found that ROI size affects the value of β. We evaluated four different square ROI sizes (1.28, 2.56, 3.2, and 5.12 cm), and we found that the larger ROI sizes yielded larger β values in the projection images.

The β values change rapidly across a single projection view; however, despite the variation across the breast, different sampling schemes (which include a variety of sampling distances and offsets) produced average β values with less than 5% variation. The particular location and number of samples used to calculate β does not matter as long as the whole image is covered, but the size of the ROI must be chosen carefully.

Keywords: Tomosynthesis, anatomic noise, power spectrum, beta, power-law

1. INTRODUCTION

Normal mammographic background ROIs have periodograms that can be described using a power law $P(f) = c/f^{\beta}$, where β ranges from 1.5 to 4.5. Anatomic noise can be the dominant noise source in a radiograph. Many researchers are characterizing anatomical noise by β, which can be measured from an image. Although β is being measured by many groups, a standardized way of estimating it does not exist. ROI sizes used in the literature range from 1.28×1.28 cm^2 to 7.2×7.2 cm^2.[1–5] Some methods allow the ROIs to overlap without restriction, while other methods use only ROIs that do not overlap at all. The frequency range over which β is calculated also varies across different studies, but it will not be addressed in this study. We will also avoid issues regarding the effects of pixel pitch.

In this study, we looked at the effect of different ROI sizes, sampling distance, and sampling offset on the average β value. We calculated β for tomosynthesis projection view and reconstructed images, and we calculated the average β across the whole image for different combinations of sampling distance and offset. Since there may be issues with averaging β across the whole image, we also investigated the effect of ROI size for individual ROIs.

Further author information:
Beverly A. Lau: E-mail: beverly@uchicago.edu, Telephone: 1 773 834 5106

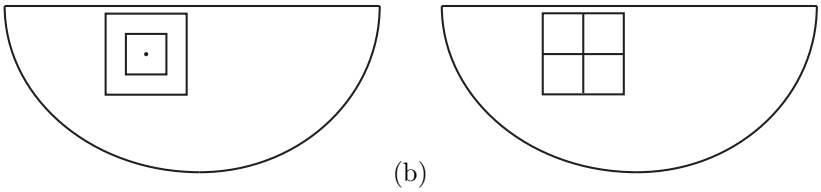

(a) (b)

Figure 1. Sampling strategies to compare the effect of ROI size on beta estimation. (a) Concentric ROIs of different sizes. (b) Four ROIs of side length $l/2$ contained in large ROI with side length l.

2. MATERIALS AND METHODS

We used clinical tomosynthesis projection images acquired with geometry described by Wu *et al.*[6] Reconstruction was done using 8-iteration MLEM. The pectoralis muscle was manually segmented and the breast was eroded using a structuring element of radius 4.8 mm. This was performed in each projection view image and in each reconstructed slice to obtain images containing regions that were uniformly thick across the breast. In some cases, visual inspection led to additional iterations of erosion in order to fully remove the non-uniformly thick regions. In the reconstructed slices, a region extending from the edges of the image in the tube direction was removed by the following amount:

$$a_p = 10(s + 20)tan(25^\circ), \tag{1}$$

where s is the slice number and the artifact area is reported in number of 100-micron pixels. The distance between the detector and the bottom of the breast was 2 cm.

Using methods from Burgess,[3] β was calculated for each region of interest (ROI) that was contained in the projected breast area, with no restriction on the amount of overlap. The image containing these β values across the whole breast shall be called the "beta map." Regions of interest were extracted from both projection view and reconstructed slice images. These square ROIs were selected in a variety of sizes (1.28, 2.56, and 3.20 cm, with a pixel pitch of 100μm) to measure the difference in average β across the breast due to ROI size selection. The mean was subtracted from each ROI and a radial Hanning window was applied to reduce spectral leakage. The modulus-squared 2D FFT was taken to yield the periodogram for each ROI. The approximated 1D power spectrum was generated through the radial average of the periodogram, and β was calculated as the slope of the 1D power spectrum between 0.15 and 0.7 cycles/mm, plotted on a log-log plot. The frequency range over which β is calculated was determined empirically in studies by Engstrom *et al.*[5]

This "beta map" was sub-sampled to simulate selection of ROIs with a variety of sampling distances. The sampling distances investigated included 0.01, 0.10, 0.20, 0.32, 0.45, 0.64, 1.28, and 1.60 cm, and the resulting beta maps were compared using average β value for the central (zero-degree) projection view image. This sub-sampling was also done with 0.05, 0.1, and 0.15 cm sampling offset to investigate the effect of sampling at a different starting places in the breast. For comparison of different sampling distance and offset methods, we averaged the power law exponent, β, across the entire zero-degree projection view image.

In addition to global averaging methods, we also investigated the comparison of β for individual ROIs. To accomplish this, we looked at two different methods: 1) comparing β for concentric ROIs

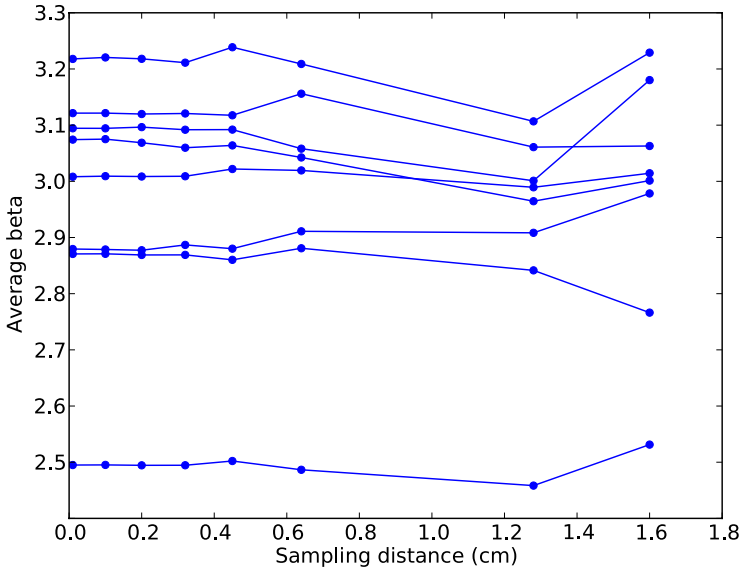

Figure 2. Beta as a function of sampling distance plotted for eight cases, showing that β is independent of sampling distance.

with a common center and which only differ in size and 2) comparing β for one large ROI with the average β for the four smaller ROIs obtained by splitting the large ROI into four quadrants (see Fig. 1). For the former method, we compared three different square ROI sizes: 1.28, 2.56, and 3.20 cm. For the latter method, we used large ROI sizes of 2.56 and 5.12 cm, which were split into four smaller ROIs measuring 1.28 cm and 2.56 cm, respectively.

We obtained 73 digital breast tomosynthesis cases from Massachusetts General Hospital. These images were the contralateral lesion-free breast images from women who were called back for diagnostic testing. Nine images were excluded because they included such objects as implants, cysts, or benign microcalcifications. This left a total of 64 cases for analysis. The images were acquired on a GE prototype system, which uses a 50-degree angular span (with center of rotation 15 cm above the breast) and 11 projection view images.

3. RESULTS

In the zero-degree projection view images of the beta maps, we compared average β values for different sampling distances and for different sampling offset amounts. We found that β varies less than 5% using different sampling strategies, so we conclude that β is independent of sampling distance and sampling offset (see Figs. 2 and 3). If the sampling distance is greater than half the size of the ROI, fewer ROIs may be extracted and the statistical uncertainty in the values increases. For this reason, we recommend sampling with at least 50% overlap.

We compared β for individual ROIs using two methods. First, we investigated three sizes of concentric ROIs (1.28, 2.56, and 3.20 cm) selected from 100 locations in the zero-degree projection view image such that each ROI completely overlapped the breast area (see Fig. 1a). The selection

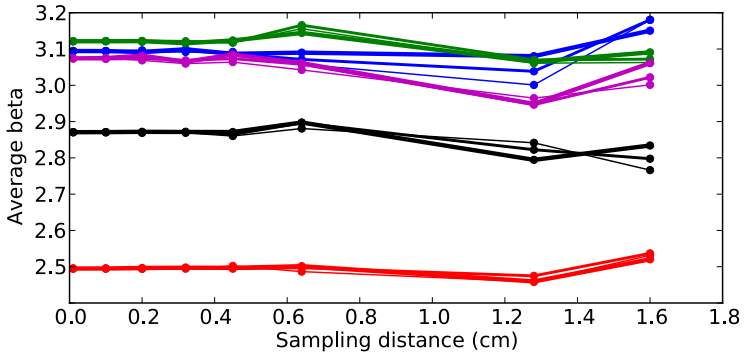

Figure 3. Beta as a function of sampling distance, plotted for three sampling offset values for five cases, showing that β is independent of sampling offset. From thin to thick equals increasing sampling offset (0.05, 0.1, 0.15 cm).

Table 1. Difference in β measured from concentric ROIs selected from 100 seed points in 64 cases. The same 100 seed points were chosen for all three pairs of ROI sizes. Note that correlation between seed points was not taken into account.

$[\text{ROI size}]_1$	$[\text{ROI size}]_2$	$< \beta_1 - \beta_2 >$	p-value	95% CI
1.28 cm	2.56 cm	-0.141	$< 2.2 \times 10^{-16}$	(-0.147, -0.135)
1.28 cm	3.20 cm	-0.134	$< 2.2 \times 10^{-16}$	(-0.140, -0.128)
2.56 cm	3.20 cm	0.007	8.3×10^{-5}	(0.0035, 0.0105)

* The critical p-value, taking into account the Bonferroni correction for multiple testing, was 0.0056.
** Zero degree projection view only.

method was repeated for the center reconstructed slices. We observed that the difference in β between any pair of sizes was statistically significant; however, the average difference in β between the two larger ROI sizes was small (0.007) compared to the other two differences (-0.141 and -0.134) (see Table 1 and Fig. 4).

We compared $< \beta >$ measured from four ROIs of side length $l/2$ to β measured from a large ROI of side length l, with the four smaller ROIs completely embedded in the larger ROI (see Fig. 1b). For 100 ROIs from the zero-degree projection view image extracted from 64 cases, we found that the average difference in β for 1.28 cm and 2.56 cm ROIs was -0.120 in the projection view images (see Table 2). For the 2.56 cm and 5.12 cm ROIs, the average difference was -0.0285 in the projection view images. It is important to note that, although these differences were statistically significant using a two-tailed paired Student's t-test, the average differences we found for the larger ROIs (2.56 cm and 5.12 cm) were very small compared with the differences we observed for the smaller ROIs (1.28 cm and 2.56 cm). The same trend was observed in the reconstructed slices (see Table 2).

In order to standardize the results presented, all paired Student's t-tests include difference calculations that are made with β from the larger ROI size being subtracted from β from the smaller ROI size. Thus, a negative mean difference indicates that the larger ROI has a larger β value than the smaller ROI does. Correlation between seed points was not taken into account in

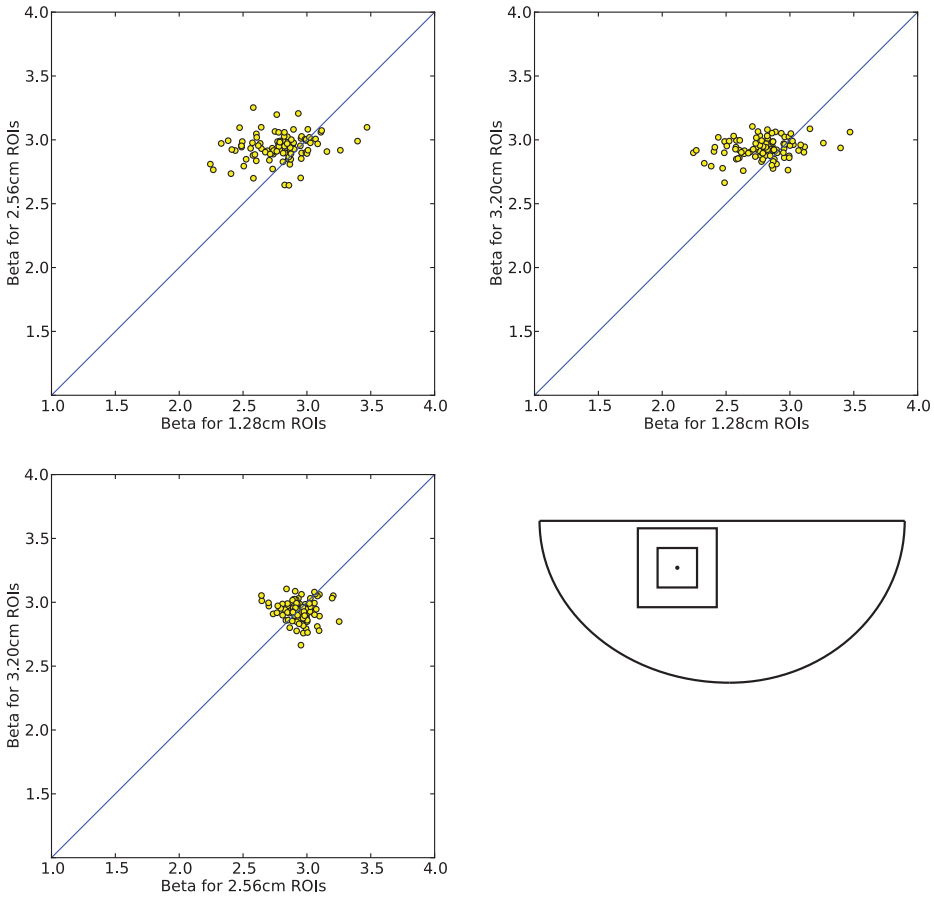

Figure 4. Beta values for concentric ROIs in the zero-degree projection view for a single case. Three sizes are compared: 1.28 cm, 2.56 cm, and 3.20 cm.

Table 2. Difference in β averaged over four ROIs compared to β for the large ROI, for 100 locations in 64 cases. The same 100 locations were used for both pairs of ROI sizes.

$[\text{ROI size}]_1$	$[\text{ROI size}]_2$	$<\beta_1 - \beta_2>$	p-value	95% CI
Projection				
1.28 cm	2.56 cm	-0.120	$< 2.2 \times 10^{-16}$	(-0.124,-0.117)
2.56 cm	5.12 cm	-0.0285	$< 2.2 \times 10^{-16}$	(-0.0306,-0.0264)
Reconstruction				
1.28 cm	2.56 cm	-0.160	$< 2.2 \times 10^{-16}$	(-0.164,-0.156)
2.56 cm	5.12 cm	-0.0641	$< 2.2 \times 10^{-16}$	(-0.0668,-0.0614)

* The critical p-value, taking into account the Bonferroni correction for multiple testing, was 0.0125.
** Zero degree projection view or center reconstructed slice only.

the statistical analysis.

4. DISCUSSION

Beta is now commonly used to characterize anatomical structure noise. Published results show that beta is reduced in the reconstructed slices as compared to the projection view images,[5] and a decrease in β corresponds to an increase in detectability of masses.[2] We have found that the method used to measure β (namely, choice of ROI size) needs to be done carefully so as not to bias the results.

In this study, we found that large ROIs (2.56, 3.20, and 5.12 cm) had larger β values than the smallest ROIs (1.28 cm), and that change in β values is negligible once the regions of interest reach a certain minimum size. We believe that the reason for this finding is related to structures in the breast being on the order of 1–2 mm in size, like Cooper's ligaments. Thus, ROI size must be chosen to match the imaging task, otherwise detectability will not be estimated accurately. Research on this topic is ongoing.

Beta seems to be independent of sampling distance and offset; however, in order to get an accurate estimate of β, it is important to sample ROIs from the entire breast.

We did not take into account correlation between ROIs in our statistical analysis. This may affect the p-values we find when such correlation is taken into consideration.

5. CONCLUSION

We have shown that the particular location and number of samples used to calculate β does not matter as long as the whole image is spanned. We also show that ROI size affects the estimation of β for ROIs that are between 1 cm and 2 cm in size. Large ROIs seem to yield consistent β values. Because of this, ROI size must be chosen carefully according to the imaging task. For microcalcifcation detection, small ROIs should be used to calculate β, and for mass detection, large ROIs should be used.

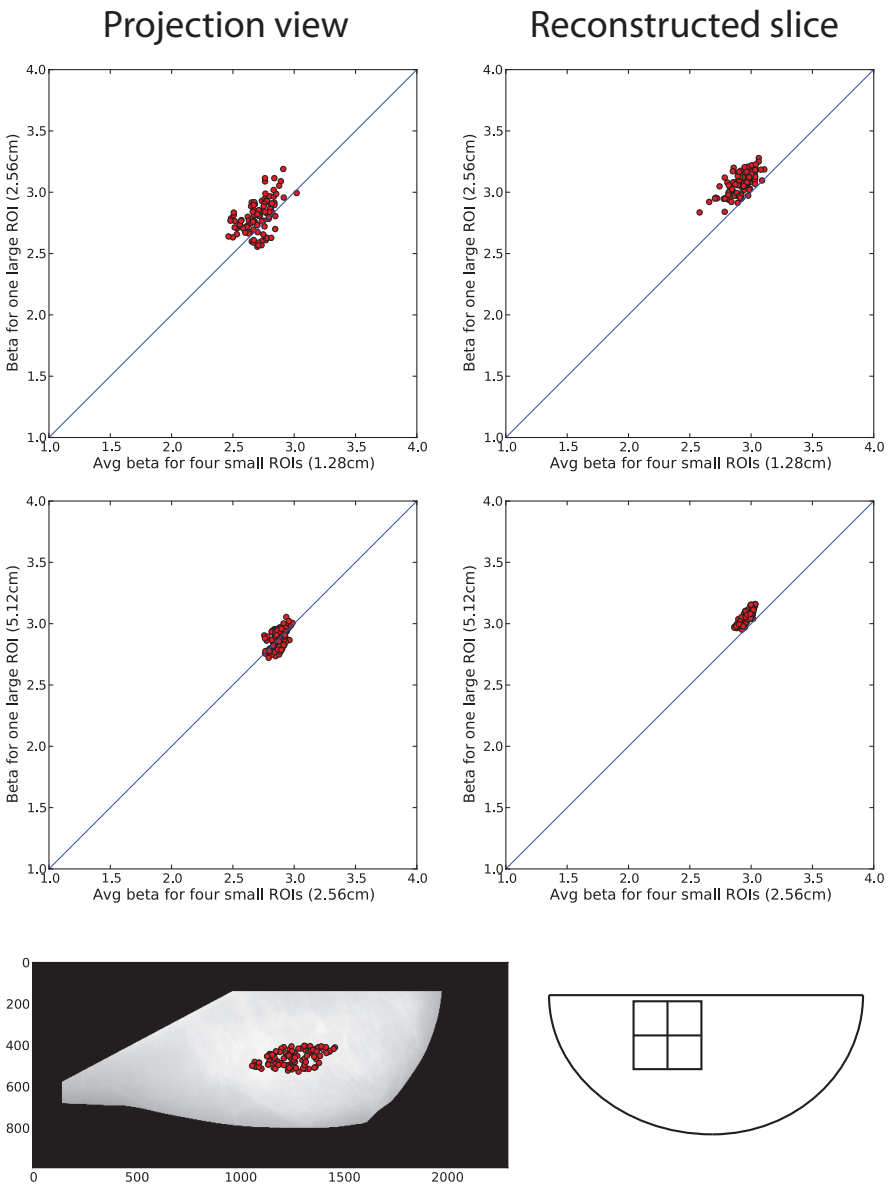

Figure 5. Beta values for ROIs and the average of their constituent quarter partitions for a single case. Data is shown for both zero-degree projection view and center reconstructed slice for a single case, with 100 ROIs per image. Top row shows data from 2.56 and 1.28 cm ROIs, and second row shows data from 2.56 and 5.12 cm ROIs.

REFERENCES

[1] J. Heine, S. Deans, R. Velthuizen, and L. Clarke, "On the statistical nature of mammograms," *Medical physics* **26**, p. 2254, 1999.

[2] A. Burgess, F. Jacobson, and P. Judy, "Human observer detection experiments with mammograms and power-law noise," *Medical physics* **28**, pp. 419–437, Jan 2001.

[3] A. Burgess, "Mammographic structure: data preparation and spatial statistics analysis," *Proceedings of SPIE* **3661**, pp. 642–653, May 1999.

[4] K. G. Metheany, C. K. Abbey, N. Packard, and J. M. Boone, "Characterizing anatomical variability in breast CT images," *Medical physics* **35**, pp. 4685–94, Oct 2008.

[5] E. Engstrom, I. Reiser, and R. Nishikawa, "Comparison of power spectra for tomosynthesis projections and reconstructed images," *Medical physics* **36**, pp. 1753–8, May 2009.

[6] T. Wu, R. H. Moore, E. A. Rafferty, and D. B. Kopans, "A comparison of reconstruction algorithms for breast tomosynthesis," *Medical physics* **31**, pp. 2636–47, Sep 2004.